Prediction of the response to antiangiogenic sunitinib therapy by non-invasive hybrid diffuse optics in renal cell carcinoma

MIGUEL MIRELES,[1,2,†] GABRIELA JIMÉNEZ-VALERIO,[2,†] JORDI MORALES-DALMAU,[1] JOHANNES D. JOHANSSON,[1,3] MAR MARTÍNEZ-LOZANO,[4] ERNESTO E. VIDAL-ROSAS,[1,5] VALENTÍ NAVARRO-PÉREZ,[6] DAVID R. BUSCH,[7] ORIOL CASANOVAS,[4] TURGUT DURDURAN,[1,8] AND CLARA VILCHES[1,*]

[1]*ICFO - Institut de Ciències Fotòniques, The Barcelona Institute of Science and Technology, 08860 Barcelona, Spain*
[2]*Computational Optics and Translational Imaging Lab, Northeastern University, Boston, Massachusetts 02115, USA*
[3]*Department of Biomedical Engineering, Linköping University, SE-581 83 Linköping, Sweden*
[4]*Tumor Angiogenesis Group, ProCURE, Catalan Institute of Oncology - IDIBELL, 08908 L'Hospitalet de Llobregat, Spain*
[5]*Digital Health and Biomedical Engineering, School of Electronics and Computer Science, University of Southampton, SO17 1BJ Southampton, UK*
[6]*Clinical Research Unit, Institut Català d'Oncologia, 08908 L'Hospitalet de Llobregat, Spain*
[7]*University of Texas Southwestern Medical Center, Departments of Anesthesiology and Pain Management, Neurology, and Biomedical Engineering Dallas, Texas 75390-9003, USA*
[8]*ICREA - Institució Catalana de Recerca i Estudis Avançats, 08010 Barcelona, Spain*
[†]*These authors contributed equally to this work*
[*]*clara.vilches@icfo.eu*

Abstract: In this work, broadband diffuse reflectance spectroscopy (DRS) and diffuse correlation spectroscopy (DCS) were used to quantify deep tissue hemodynamics in a patient-derived orthotopic xenograft mouse model of clear cell renal cancer undergoing antiangiogenic treatment. A cohort of twenty-two mice were treated with sunitinib and compared to thirteen control untreated mice, and monitored by DRS/DCS. A reduction in total hemoglobin concentration (THC, $p = 0.03$), oxygen saturation (SO_2, $p = 0.03$) and blood flow index (BFI, $p = 0.02$) was observed over the treatment course. Early changes in tumor microvascular blood flow and total hemoglobin concentration were correlated with the final microvessel density ($p = 0.014$) and tumor weight ($p = 0.024$), respectively. Higher pre-treatment tumor microvascular blood flow was observed in non-responder mice with respect to responder mice, which was statistically predictive of the tumor intrinsic resistance ($p = 0.01$). This hybrid diffuse optical technique provides a method for predicting tumor intrinsic resistance to antiangiogenic therapy and could be used as predictive biomarker of response to antiangiogenic therapies in pre-clinical models.

1. Introduction

Renal cell carcinoma (RCC) is one of the most common urinary tract malignancies, with more than 430,000 new cases reported worldwide in 2022, accounting for 2.2% of total new cancer cases [1]. Clear cell renal cell carcinoma (ccRCC) is the most prevalent subtype of RCC, characterized by high metastasis and mortality rates [2]. ccRCC tumors are largely insensitive to chemotherapy and radiotherapy, and nephrectomy remains the standard of care for localized ccRCC. However around 20% of patients are already diagnosed at metastatic stages (mRCC), and approximately 30% of patients eventually develop metastases after surgery [3]. The difficulties

in treating metastatic lesions and the low 5-year survival rates have motivated the development of new treatment strategies for mRCC over the last decades, particularly targeting the highly vascular nature of ccRCC tumors. Indeed, therapies aimed at inhibiting angiogenesis to halt tumor progression have been integrated into clinical practice guidelines for mRCC management [4].

Among antiangiogenic agents used for mRCC, sunitinib stands out as the standard first-line treatment for patients with favorable to intermediate risk [4] and it remains as the comparative treatment in clinical studies of new drugs [2]. Sunitinib acts by inhibiting the activity of the proangiogenic vascular endothelial growth factor (VEGF), which significantly decreases tumor angiogenesis and, in turn, inhibits tumor growth [5–7]. In spite of the demonstrated therapeutic benefits of sunitinib over other treatments in terms of progression free survival and drug tolerance, resistance to sunitinib is still the major obstacle in mRCC management: almost 30% of patients present intrinsic resistance, and even those with good initial responses might acquire resistance within 6-15 months of therapy [8,9]. How patients develop intrinsic and acquired resistance still remains unclear and many different and multiple mechanisms have been proposed, but there is also a lack of predictive biomarkers of therapy resistance and response.

In the last years, several studies have tried to validate clinical parameters [10], adverse effects [11] and circulating biomarkers as secreted VEGF-A and IL-8 [12], associated with sunitinib resistance or better clinical outcomes. However, these predictors are addressed at the systemic level rather than directly imaging tumor microvasculature properties and the hemodynamic changes hypothesized to occur during treatment. The kinetics and magnitude of those changes might be indicative of either the tumor response to antiangiogenic agents or of the adaptive process developed by the tumor to become therapy resistant [13]. Advanced imaging techniques such as PET/MRI and PET/CT, that allow a combined anatomic, metabolic and physiological imaging of renal tumors, have shown promising utility for predicting responses and resistance to sunitinib treatment in patients with advanced RCC [14,15]. Yet, these methods are costly and require the use of radiation or contrast agents which are not always tolerated by RCC patients. Therefore, to date, there are no validated, non-invasive tools for the monitoring of tumor microvasculature prior or during therapy that could help clinicians discriminate which patients would benefit from treatment, avoiding the use of ineffective therapies [16].

In this sense, diffuse optical techniques working mainly in the near-infrared emerge as potential set of tools for longitudinal and non-invasive monitoring of tissues, providing relevant information on hemodynamics, physiology and tissue structure. These techniques, namely diffuse correlation spectroscopy (DCS) and diffuse reflection spectroscopy (DRS), differ from other techniques in their ease-of-use, safety for multiple applications and their non-invasiveness [17]. In the last decades, we and others have demonstrated the utility of optical monitoring of tumor hemodynamics to predict therapeutic efficiency in many different oncology settings, such as neoadjuvant chemotherapy, radiation therapy and photodynamic therapy, in both pre-clinical and clinical studies [18–28]. In particular, and of relevance to this work, the effectiveness of combining DCS and DRS was previously demonstrated to measure tumor microvascular blood flow, total hemoglobin concentration and blood oxygenation changes in a murine model of ccRCC under antiangiogenic treatment targeting vascular endothelial growth factor receptor 2 (VEGFR-2) [21]. Results revealed a correlation between early changes in hemodynamics with therapeutic outcome, paving the way to use such techniques to validate prognostic biomarkers in antiangiogenic treatments.

In the present work, we use these diffuse optical techniques to explore the potential for the prediction of response to the gold-standard sunitinib antiangiogenic drug, in an orthotopic xenograft of ccRCC mouse model. To this end, we quantify pre-treatment tumor hemodynamics and their early changes during treatment as potential biomarkers to predict therapy outcome. We have identified the pre-treatment total hemoglobin concentration (THC) and blood flow

index (BFI) as a potential set of predictive biomarkers of the therapy outcome, whereas the early changes in physiological parameters are predictive metrics of the final therapy effects. Ultimately, this work may allow to envision strategies to use these non-invasive biomarkers in order to optimize therapy selection for advanced cancer patients and develop personalized treatments.

2. Method

2.1. Patient-derived orthotopic xenograft (PDOX) models of renal cancer

Histologically-intact fragments from primary biopsies of human clear cell RCC tumors (ccRCC, named REN108) were obtained from the Vall d'Hebron Hospital under protocols approved by local ethics committee (CEIC approvals PR322/11 and PR (AG) 240/2013). One of these fragments, from a single patient, was surgically implanted orthotopically in the kidney (original neoplastic organ) of an athymic male nude mouse (primary mouse) (Envigo Laboratories) [29] and left to grow. Once the tumor achieved a sufficiently large volume, the primary mouse was sacrificed to excise the tumor, which was then sectioned into several fragments of approximately 1 mm^3 volume. Each one of these fragments was implanted on the kidney of a group of mice, from which a subpopulation was chosen for our study and left to grow according to our protocols (See Section 2.2). The rest of the mice were reassigned as new primary mice to perpetuate the tumor line. All animal experiments were conducted at IDIBELL's Animal Facility. All procedures were approved by the institution's Animal Research Committee and the corresponding department by the regional government (approval DMAH #4899).

2.2. Treatment plan

Tumor growth was evaluated by palpation once per week, and when tumors reached a volume of 1000 mm^3, mice were randomized into two groups: treatment and control. The treatment group (n = 22) received sunitinib (S-8803 Sunitinib Malate, LC Labs, USA) at a dosage of 40 mg/kg/day, administered daily by oral gavage during 21 days. The control group, i.e., without antiangiogenic treatment, (n = 13), received carboxymethyl cellulose vehicle formulation in the same dosage, administration route and frequency.

Mice were monitored over a period of twenty-one days in which they were fed *ad libitum* and maintained in a specific pathogen-free environment at the animal facility. Tumor growth was followed by palpation twice a week and the treatment was considered effective until primary tumors increased by 25% their initial volume. At the end of the treatment, mice were sacrificed, and tumors were extracted and weighted. Final tumor volume was estimated by water displacement in a graduated cylinder. Tumors were then processed for immunohistology analysis.

2.3. Immunohistochemical staining and quantification

Frozen or formalin-fixed paraffin-embedded (FFPE) tumor sections were stained with hematoxylin-eosin (H&E) and immunohistochemistry techniques as previously described [30]. Rabbit anti-cluster of differentiation 31 (CD31, Abcam, ab28364) and EnVision system of labeled polymer-horse radish peroxidase (HRP) anti-rabbit IgG (DakoCytomation, Agilent Technologies, Santa Clara, USA) were used as primary and secondary antibodies, respectively. 4'-6-diamidino-2-phenylindole (DAPI, Sigma, 0929) was used for nuclear counterstaining, and finally tissue sections were mounted in DPX medium (Merck, 1005790500). To quantify CD31 positivity, four to six hotspot fields in viable tissue zones at 20X magnification were captured for each tumor. Microvessel density (MVD) was obtained by counting the number of CD31-positive vessels in each field using a Nikon Eclipse 80i microscope (NIKON-801 DS-Ri1, NIKON, Japan), whereas the percentage of necrosis (NP) was calculated as the ratio of the necrotic-pixel-area/total-image-pixel-area multiplied by hundred, using ImageJ software (version 1.5.2, National Institutes of Health, USA) [31].

2.4.   Hybrid optical setup

A schematic of the hybrid DRS/DCS contact setup and examples of the acquired optical data are shown in Figs. S1 and S2 of the Supplement 1. A detailed description of the hybrid diffuse reflectance spectroscopy (DRS) and diffuse correlation spectroscopy (DCS) device can be found in Farzam *et al.* [21] and in Mireles *et al.* [32]. Briefly, the DRS system consisted of a continuous wave 250 W broadband illumination lamp (QTH source model 66499, lamp model 6334 NS, Oriel Instruments, Newport Corporation, USA) coupled to two 400 μm multimode fibers to deliver light to the tissue. Diffuse reflected light was collected through six multi-mode fibers at distances ranging from 0.25 to 0.5 cm from the illumination point. The detected light was spatially and spectrally resolved by a two-dimensional spectrometer (Acton Insight with CCD PIXIS eXcelon 400B, Princeton Instruments, USA) over a wavelength range from 600-1000 nm.

The DCS system consisted of a long coherence length 785 nm laser (DL785-120-S, CrystaLaser, USA) as a light source, the diffuse reflected light was collected by single mode fibers at eight source-detector separations ranging from 0.25 to 0.5 cm. The collected photons were detected by single photon avalanche photodiodes (SPCM-ARQH-14, Excelitas Technologies, USA). The output photon counts were fed into a correlation board (Correlator.com, USA) to compute the self-normalized intensity autocorrelation function for each source-detector separation. Post-processing of the signals was performed for retrieving the blood flow index (BFI). The set of fibers for light delivery and collection of both techniques (DRS and DCS) were assembled in a contact probe. Optical data was collected and analyzed offline using the semi-infinite approximations to the photon and correlation diffusion equations as described in Durduran *et al* [17]. and Farzam *et al.* [21] to retrieve the tissue optical properties, which were then used to estimate microvascular, total hemoglobin concentration (THC), tissue/blood oxygen saturation (SO_2) and BFI following the data processing pipelines employed in our previous publications [21,32].

Our probe design allows us to achieve a theoretical mean light penetration depth of about 0.25 cm [33]. This sampling depth has been previously validated by our group [21,32] and others [20,34,35] to provide enough penetration depth to sample representative volumes regions of the tumor. Given the expected tumor volume increase over the treatment course, we note that we sampled over different regions across the tumor (see Section 2.5) which adds to the variability of the data.

2.5.   Diffuse optical measurement protocol

Prior to and during the optical data acquisition, mice were anesthetized with a mixture of isoflurane and oxygen (4% isoflurane and 2 L/min of oxygen for induction, and 2% isoflurane and 2 L/min of oxygen for maintenance). Mice body temperature was stabilized at 34°C and monitored by means of a heating blanket with a rectal temperature sensor feedback (PS-03, PhysioSuite, MouseSTAT Pulse Oximeter, Kent Scientific, USA).

Using the device described in Section 2.4, optical data was collected non-invasively from each mouse by positioning the contact hand-held probe at two different locations: shoulder and tumor. In the shoulder, data was collected five times from the same position. In the tumor, five different positions were probed, where the last one corresponded to the probe placed at the top center of the tumor and the rest, in reference to the top one, the surrounding cardinal points. Total acquisition time for the ten measured locations lasted around ten minutes. Data was acquired daily starting before the treatment administration on the day of the treatment ("Day 0") for six days (until "Day 5"), and on days seven, ten, fourteen, seventeen and twenty.

For every optical measurement, the contact hand-held probe was removed and repositioned for achieving better statistical results including the test/re-test variability (e.g., due to the probe-tissue coupling and pressure). To minimize their impact, in addition to the self-calibration procedures that were detailed, only optical data from every channel at each position that are at least 3x above the mean dark level was utilized while trying to maintain similar contact surface,

pressure and orientation across measured positions over time. In the shoulder position, marginal adjustments were required due to homogeneity of the region resulting in an overall reduced physiological variability for the whole treatment period (Table S1). However, adjustments in the probed locations for the tumor area were needed over the course of measurements due to the heterogeneous tumor growth. We note that such adjustments did not represent a significant impact in the recovered physiological values, showing a slightly elevated inter-tumor variability for both the treated (Table S1, THC: ± 30 μM, SO$_2$: $\pm 9\%$ and BFI: 1×10^{-8} cm^2 s^{-1}) and control (Table S1, THC: ± 35 μM, SO$_2$: $\pm 11\%$ and BFI: 2×10^{-8} cm^2 s^{-1}) mice over the course of treatment compared to the pre-treatment measurements (Table 1, THC: ± 30 μM, SO$_2$: $\pm 9\%$ and BFI: $\pm 1.3 \times 10^{-8}$ cm^2 s^{-1}) and illustrated by the confidence intervals (CI) in Fig. 4.

Table 1. Pre-treatment tissue characterization. The estimated pre-treatment tissue hemodynamics by measured location and treatment group and their statistical significance. Data expressed as mean ± standard deviation.

		THC [μM]	SO$_2$ [%]	BFI [10^{-8}cm^{2}s^{-1}]
A. Measured positions	Tumor	76 ± 30	75 ± 9	2.8 ± 1.3
	Shoulder	39 ± 5	52 ± 5	2.0 ± 0.9
	p-value	< 0.01	< 0.01	< 0.01
B. Therapy group	Treated-Tumor	77 ± 27	75 ± 7	3.0 ± 1.2
	Control-Tumor	73 ± 36	74 ± 12	2.5 ± 1.3
	p-value	0.72	0.78	0.25
	Treated-Shoulder	38 ± 4	51 ± 5	2.1 ± 1.0
	Control-Shoulder	40 ± 7	53 ± 5	1.7 ± 0.8
	p-value	0.20	0.31	0.25

2.6. Classification of the therapy response

We have classified the animals according to the antiangiogenic effect on the tumor volume obtained by palpation, which provides a fast, cost-effective, and consistent volume estimation of irregularly-shaped tumors, even those embedded deeply within tissue. This method uses the fingertips to protrude the tumor from the surrounding tissues by applying a pinching motion while applying downwards pressure at the tumor margins, facilitating a more accurate estimate of the tumor volume by better revealing the full extent of the tumor mass. This method was validated (unpublished results) within our laboratory by comparing against tumor volumes measured *ex vivo*, demonstrating that an experienced, single operator can achieve very good correlation against true tumor volume. The mice in the treated group were classified into two groups: (i) the responder group where the tumor volume did not increase more than 25% with respect to its initial volume, and (ii) the non-responder group where the tumor volume increased more than 25% with respect to its initial volume. These groups formed the therapy outcome groups.

2.7. Statistical analysis

Data analysis was performed in R statistical software (version 3.3.2, R Foundation for Statistical Computing, Austria). Statistical differences in tumor volume, weight, microvessel density and necrosis percentage were assessed with Mann-Whitney-Wilcoxon rank sum test. Statistical differences in the mean values of the estimated parameters distributed across treatment and therapy groups were conducted using a non-parametric Kruskal-Wallis test (denoted as p) and bootstrap (p$_{bs}$) random sampling with replacement. The longitudinal statistical analysis between the groups was done using a linear mixed-effect (LME) method to account for repeated measures. The normal distribution of the pre-treatment estimations was tested by means of a Jarque-Bera

test (p_{jb}). The Pearson's correlation coefficient (r) was employed to quantify the linear correlation agreement between the early changes in the tissue hemodynamics and the *ex vivo* histology results. Finally, uni- and multi-variate analyses were used to assess the statistical power of the pre-treatment tumor hemodynamics to classify the therapy response. In this regard, to enhance the contrast among groups, the data was transformed using the z-score metrics described in Busch *et al.* [36] A receiver operating characteristic (ROC) curve was used to evaluate the sensitivity and specificity of the classification. The area under the curve (AUC) was used to assess the performance of the classification method. Data dispersion was evaluated through interquartile range (IQR) metric. All the statistical tests were considered significant at $\alpha \leq 0.05$ for rejecting the null hypothesis.

3. Results

3.1. Treatment associated changes in tumor volume and weight

On average, patient-derived orthotopic xenograft (PDOX) tumor volume allowed to identify therapy response. In specific, tumor volume showed a statistically significant difference ($p < 0.01$) between control and treated mice (Fig. 1(A)). Nevertheless, tumor volume of treated mice showed a heterogeneous response, hence, allowing us to discriminate those that were responding to treatment (Fig. 1(B), in red, n = 14) from non-responders and/or intrinsically resistant tumors (Fig. 1(B), in blue, n = 8). No differences were observed between control and non-responders ($p = 0.83$), while the responder group was different from both the control and the non-responder group ($p < 0.01$). The underlying mechanism behind the heterogeneous tumor response (resistant vs sensitive) is unclear; however, it is hypothesized that the heterogeneity of cells within the tumor might give rise to such phenomena [37,38]. Likewise, given the nature of our PDOX model, the observed proportion of resistant cases (n = 8) with respect to the total treated mice (n = 22) might come from the heterogeneities in the primary biopsies from the human tumor being transferred to our animal model. We note that the proportion of resistant to sensitive cases in this study is in agreement with literature observations [8,9].

At the end of the treatment, group discrimination was further confirmed with differences in both tumor volume (Fig. 1(C)) and weight (Fig. 1(D)). Final tumor volume was found to be significantly lower ($p < 0.001$) in responders (1050 ± 138 mm^3, IQR = 200, Fig. 1(C), in red) compared to non-responders (1950 ± 399 mm^3, IQR = 650, Fig. 1(C), in blue), as well as between the responders and the controls (2200 ± 594 mm^3, IQR = 500, Fig. 1(C), in black, $p < 0.001$). However, final tumor volume was not different ($p = 0.14$) among non-responders and controls. Likewise, tumor weight revealed differences between responders (0.90 ± 0.17 gr, IQR = 0.275, Fig. 1(D), in red) and both controls (2 ± 0.53 gr, IQR = 0.4, Fig. 1(D), in black, $p < 0.001$) and non-responders (1.55 ± 0.27 gr, IQR = 0.35, Fig. 1(D), in blue, $p < 0.001$). Tumor weight was also significantly different ($p = 0.03$) between control group and non-responders. In Supplemental Figure S3, representative images of tumors from control, responder and non-responder groups can be found.

3.2. Histological evaluation of the response to the sunitinib treatment

To investigate the histological response to the sunitinib treatment, tumor tissue sections were analyzed as described in Section 2.3. No significant differences ($p > 0.05$) in the microvessel density (MVD, Fig. 2(A)) were found between controls (20.25 ± 8.04 vessels/mm^2) and non-responders (16.5 ± 3.76 vessels/mm^2); however, in responder tumors, where sunitinib impairs tumor growth through angiogenesis inhibition, a significantly decreased density of the tumor microvasculature (9.2 ± 1.94 vessels/mm^2) was observed compared to both controls ($p < 0.001$) and non-responders ($p < 0.001$). Tumor necrosis was similar ($p \geq 0.05$) in all therapy outcome
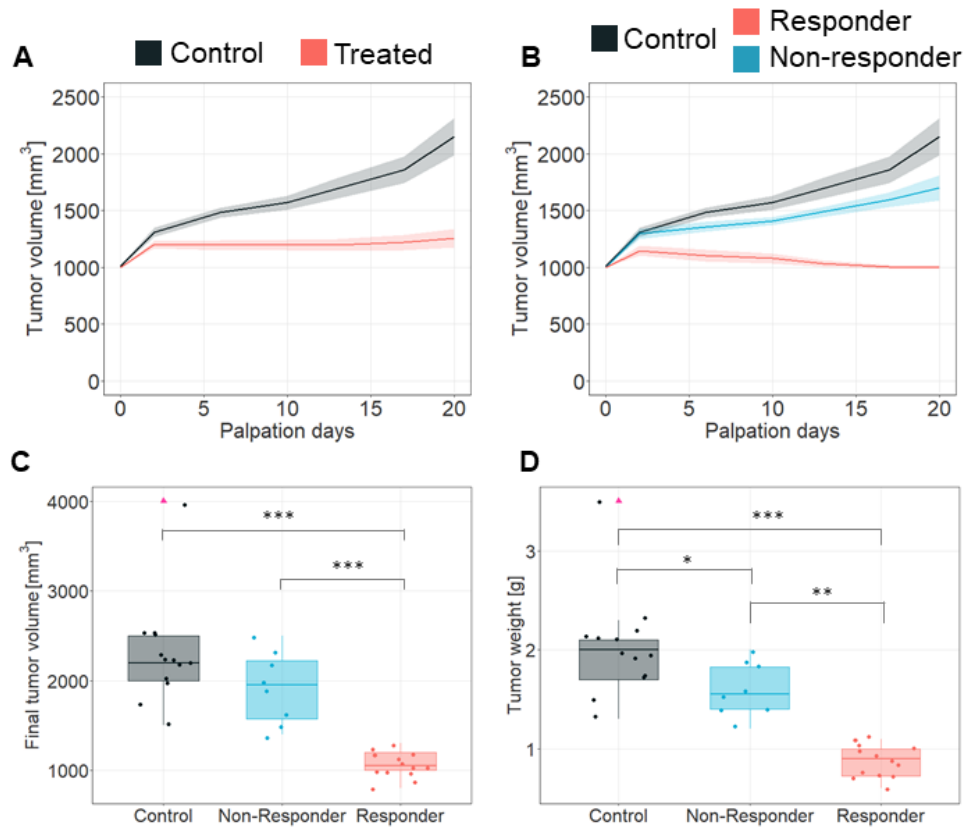
Fig. 1. Effects of sunitinib treatment in REN108 RCC PDX tumor. A. Tumor volume progression measured by palpation in REN108 RCC orthotopic xenografts tumors. Solid lines represent the mean tumor volume over time whereas the ribbon area denotes the standard error of the mean (SEM). n = 13 controls and 22 treated animals. **B.** Tumor volume progression measured by palpation in REN108 RCC orthotopic xenograft tumors. According to the therapy response, mice were classified in controls (black line), responders (red line) and non-responders (blue line). Solid lines represent the mean tumor volume over time whereas the ribbon area denotes the 95% confidence interval (CI). n = 13 controls, 14 responders and 8 non-responders animals. **C.** Final tumor volume and **D.** Tumor weight measured at sacrifice. Data from n = 13 controls, 14 responders and 8 non-responder animals. Medians and IQR for each group and parameters are shown. Mann-Whitney-Wilcoxon rank sum test are shown with * for $p \leq 0.05$, ** for $p \leq 0.01$ and *** for $p \leq 0.001$. Pink triangles indicate outlier points.

groups (Fig. 2(B)). Supplemental Figure S4 shows representative images of immunostained tissue slices for each group.

3.3. Diffuse optical results

DCS/DRS were used to assess sunitinib-derived hemodynamic changes in tumor and shoulder (Fig. 3). In general, THC, SO_2 and BFI (Fig. 3(A), C and E, and Supplement 1) were observed to be affected by sunitinib treatment in the tumor, whereas healthy muscle hemodynamics remained unaltered during treatment (Fig. 3(B), D and F, and Supplement 1). In particular, treated tumors showed, compared to controls, a statistically significant reduction in THC (Fig. 3(A), p = 0.03, $p_{bs} \leq 0.048$) from day seven of treatment onward; in SO_2 (Fig. 3(C), p = 0.03, $p_{bs} \leq 0.03$) from
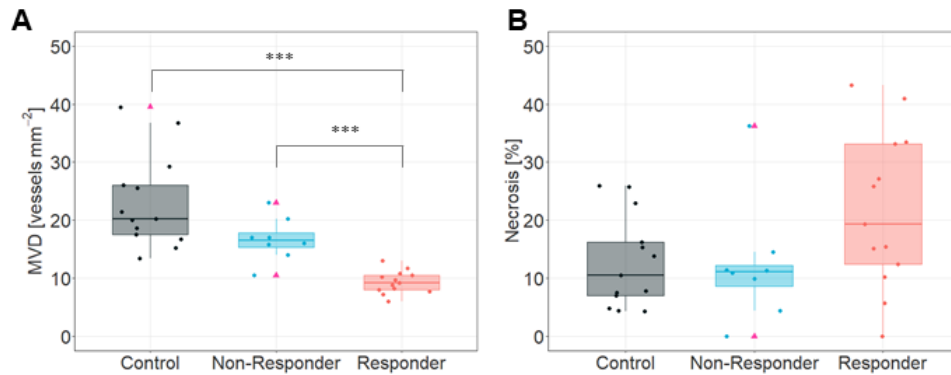
Fig. 2. Tumor *ex vivo* characterization and histology. **A.** Microvessel density quantification (MVD, vessels per mm^2). **B.** Tumor necrosis quantification (% of necrosis). Data from n = 13 controls, 14 responders and 8 non-responder animals, 4 images per sample section were captured and quantified. Medians and IQR are represented. Mann-Whitney-Wilcoxon rank sum test are shown with *** for p ≤ 0.001. Pink triangles indicate outliers.

day ten of treatment; and in BFI (Fig. 3(E), p = 0.02, p_{bs} ≤ 0.02) from day fourteen onward. In contrast, none of the parameters measured on the shoulder location showed changes (Fig. 3(B), D and F, with p = 0.87, p = 0.71 and p = 0.52 for THC, SO$_2$ and BFI, respectively), indicating the specific VEGF-targeting effect of the therapy in the tumor without systemic implications.

Moreover, when animals were further split as responders and non-responders, no statistical differences were observed in their longitudinal trends among groups in either THC (Fig. 4(A), p = 0.46) nor BFI (Fig. 4(E), p = 0.68) at the tumor location. Tumor SO$_2$, however, was higher (p = 0.04) in the non-responder group with respect to the responder with a statistically significant difference from day fourteen (p = 0.04, p_{bs} ≤ 0.04) onwards (Fig. 4(C)). Controls and non-responders showed similar SO$_2$ values (p = 0.77). The shoulder muscle did not reveal any significant differences among therapy outcome groups in any hemodynamic parameter (Fig. 4(B), D and F, with p = 0.69, p = 0.51, p = 0.34 for THC, SO$_2$ and BFI respectively).

In addition to the longitudinal vascular changes observed during the treatment period, early tumor hemodynamic changes were further investigated as potential biomarkers to predict therapy effects. As shown in Fig. 5, the changes in BFI (ΔBFI) and THC (ΔTHC) at day three after therapy (Δ = Day 3 - Day 0) were correlated with the histological tumor MVD (Fig. 5(A), r: 0.42, p = 0.014) and the extracted tumor weight (Fig. 5(B), r: 0.39, p = 0.024), respectively.

3.4. Diffuse optical prediction of therapy outcome

Prior to therapy initiation, all measurements of THC, SO$_2$ and BFI in the tumor were consistently higher (p ≤ 0.01) than those in the healthy tissues as represented by the shoulder muscle measurements (Table 1(A)); in agreement with the known anabolic processes taking place during angiogenesis to supply oxygen and nutrients to the tumor. Nevertheless, the full set of estimated hemodynamic parameters were similar between the treated and control groups both in the tumor and in the shoulder positions (Table 1(B)); thus, reflecting the biological process proper of the tumor growth. We note that, owing to the enhanced sensitivity of DRS technique to the microvascular tissue physiology, with a roughly weight of 2/3^{rds} towards the venous compartment, low tissue SO$_2$ percentages are observed and in agreement with previously reported DRS validation studies [23,39].

The pre-treatment (day zero) tumor hemodynamics in control, non-responder and responder groups showed differences among them, but data showed a skewed distribution (data not shown). Therefore, values were log-transformed to achieve a normal distribution (Fig. 6). Pre-treatment
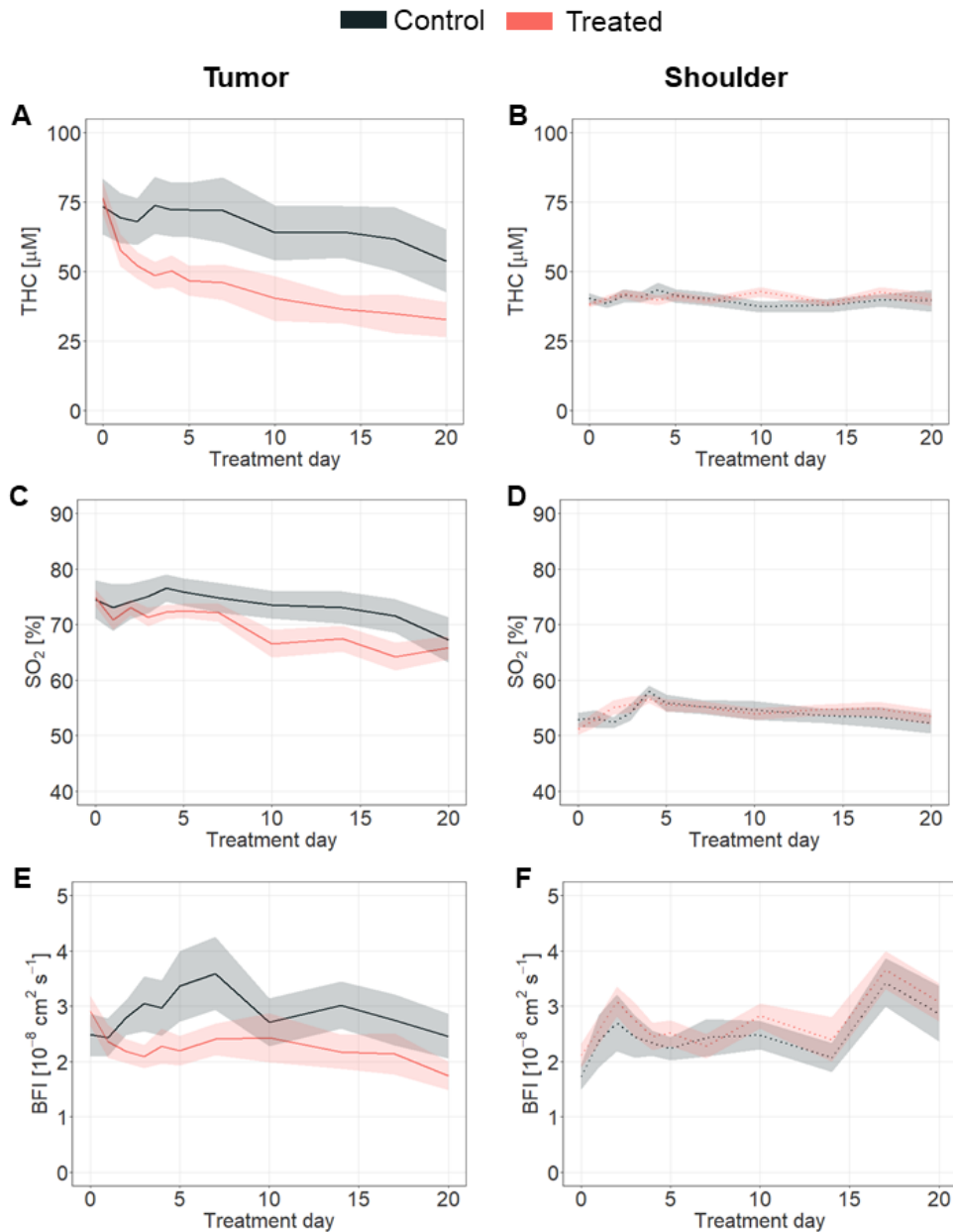
Fig. 3. Therapy effects on tissue hemodynamics. In the tumor location (left column); **A.** THC, **C.** SO_2 and **D.** BFI hemodynamics of the treated group (red, n = 22) were statistically different (p ≤ 0.01) from those of the control (black, n = 13) group. In the shoulder location (right column, panels **B., D., E.**); no statistically significant difference between the treated and control groups in any hemodynamics parameter (p ≥ 0.05) was observed. All values in the figures are Mean ± SEM.

log-transformed values of THC (Fig. 6(A)) and SO_2 (Fig. 6(B)) in the tumor did not show any statistically differences between any group (Supplemental Table S2), while BFI (Fig. 6(C)) was statistically significant different (p = 0.01, p_{bs} < 0.05) between responders and non-responders. However, both groups were not different from controls (Supplemental Table S2).

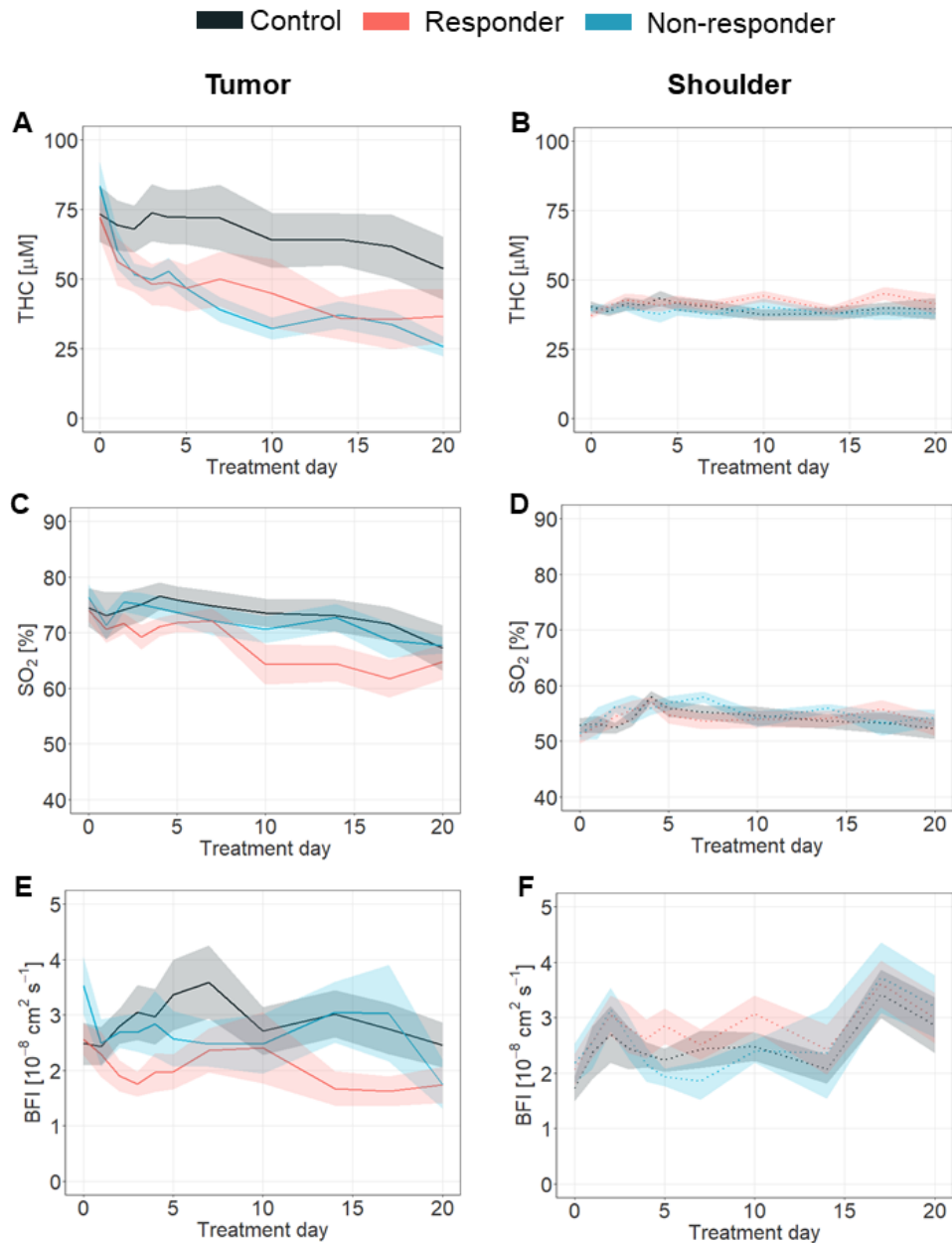**Fig. 4. Therapy outcome discrimination by the estimated tissue hemodynamics**. In the tumor location (left column); **A.** THC, **C.** SO$_2$ and **E.** BFI hemodynamics of the responder (red line), non-responder (in blue) and control (in black) groups are shown. In the right column, panels **B.**, **D.**, **E.** show THC, SO$_2$ and BFI values obtained in the shoulder location. All values in the figures are Mean ± SEM.

This data suggested the possibility that pre-treatment BFI could define or predict therapy outcome, so prediction power of this variable was further evaluated in a receiver operating characteristics (ROC) curve analysis (Fig. 7). Log-transformed BFI fitted a statistically significant model (p = 0.01, p$_{bs}$ ≤ 0.03) with an area under the curve (AUC) of 0.81 (Fig. 7(A)). Consistently,
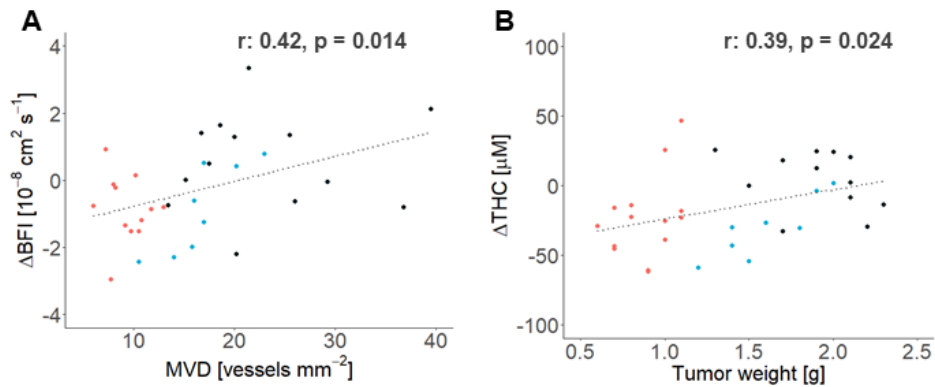
Fig. 5. Early tissue hemodynamics changes predict the antiangiogenic therapy effect. The changes at day three after treatment (Δ = Day 3 - Day 0) of the *in vivo* recovered blood flow index (BFI) and total hemoglobin concentration (THC) parameters were observed to correlate with the *ex vivo* tumor characteristics: **A.** The initial tumor BFI change was observed to correlate with the histology recovered tumor micro vessel density (MVD). **B.** The initial tumor THC was observed to correlate with the extracted tumor weight (TW). Individual data points for responders are shown in red, non-responders in blue and controls in black. r is the Pearson correlation coefficient.
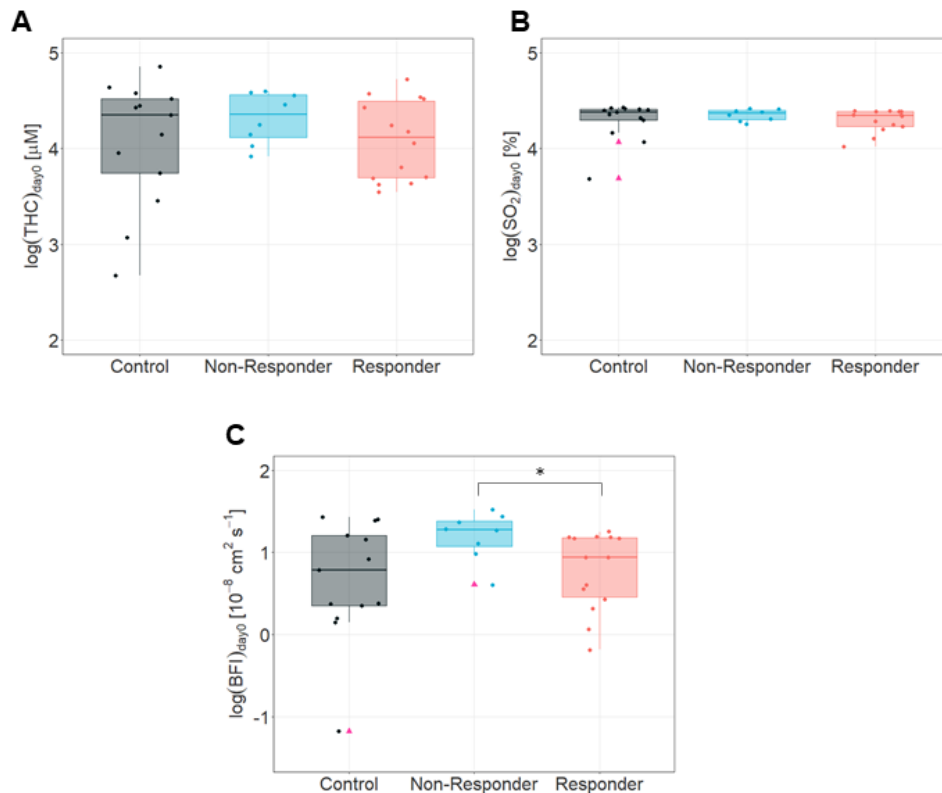

Fig. 6. Pre-treatment discrimination of therapy outcome. The log transformed values for **A.** THC, **B.** SO$_2$ and **C.** BFI, at pre-treatment day in controls, non-responders and responders. Median and IQR are represented. Pink triangles indicate outliers. * is for $p < 0.05$.
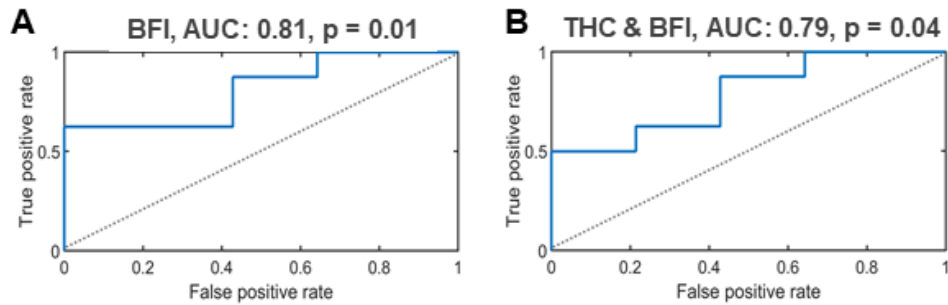
Fig. 7. Therapy outcome classification based on pre-treatment tumor hemodynamics. The therapy outcome was classified by a binomial logistic regression of the pre-treatment tumor hemodynamics. **A.** The univariate binomial logistic regression model of the tumor BFI. **B.** The multivariate binomial logistic regression model of the combined tumor THC & BFI parameters.

log-transformed pre-treatment tumor THC and SO_2 univariate models were not statistically significant ($p = 0.15$ and $p = 0.14$, respectively, data not shown). In a multivariate analysis (Fig. 7(B)), the combined contribution of the log-transformed pre-treatment tumor THC and BFI demonstrated a statistically significant model ($p = 0.04$, $p_{bs} \leq 0.047$) with an AUC of 0.79. The other multivariate models (THC & SO2 and BFI & SO2) were not statistically significant ($p = 0.32$ and $p = 0.052$, respectively) (data not shown). A summary of the uni- and multi-variate binomial logistic regression of the tumor hemodynamics at the pre-treatment time point for the therapy outcome classification is provided in Supplemental Table S3.

4. Discussion

During the last decade a high heterogeneity of the tumor response to antiangiogenic therapy have been described in the clinics [37]. Currently, there are no validated biomarkers to accurately predict which patients will benefit from anti-vascular endothelial growth factor (VEGF) therapies [40]. Therefore, it would be of great relevance to find evidence that could identify new predictive biomarkers of response, particularly early-response, which, in turn, could help in the selection of the therapy, in prevention of therapeutic failures and in avoiding the associated toxicities. In this work, diffuse optical techniques have been employed to investigate the baseline values and the evolution of the tissue hemodynamics as biomarkers to aid the understanding of the therapeutic effects of antiangiogenic therapy in an orthotopic xenograft mouse model of clear cell renal cell carcinoma (ccRCC) derived from a human tumor sample [41,42]. As therapeutic agent, we used the clinical standard antiangiogenic drug sunitinib, which is a multitargeted receptor tyrosine kinase that primarily blocks the vascular endothelial growth factor receptor to inhibit new blood vessel formation [43,44].

As expected, the tumor volume evaluated by palpation over time was observed to be statistically significantly different between the treated and control groups. However, in some treated mice, the tumor volume was not successfully controlled by the antiangiogenic drug and continued to grow during the experiment. In other words, some mice displayed intrinsic resistance characteristics despite having received therapy. This observed behavior resembled the heterogeneous response reported both in human [45–47] and pre-clinical [48] studies which has been associated to several tumor resistance mechanisms [49,50], and allowed us to classify mice as responders and non-responders.

The histological characterization and immunohistochemistry analysis of the tumor samples confirmed the similarity between the non-responder and control groups whereas the responder group was observed to be systematically different from the others. These results might arise from

the fact that the therapeutic mechanism of sunitinib is based on the inhibition of the neovasculature formation. This could slow down the tumor growth and reduce the final tumor volume and weight in the responder group, while the non-responders might be capable of overcoming the vascular trimming targeted by sunitinib drug through several mechanisms of resistance [29,49,9], resulting in a similar behavior as non-treated tumors. Despite the observed group differences in microvessel density, the extent of tumor necrosis was similar among controls, non-responders and responders. This might be due to the combination of two factors. On one hand, the vascular trimming in responders group deprives the tumor from oxygen and nutrients supplied by the bloodstream [51], thus leading to the formation of necrotic areas. On the other hand, the larger tumor volume of controls and non-responders could lead to the natural formation of necrotic regions due to the lack of vascular support, reaching similar values as in the responder group.

Taking advantage of this heterogeneous response model, which resembles the clinical scenario of antiangiogenic therapy response, diffuse optical techniques were used to investigate tissue hemodynamic changes induced by this therapy, aiming to find a predictive parameter that could be used as a new biomarker to predict patient outcome. The non-invasive, practical nature of the diffuse optical platform allowed us to monitor the *in vivo* tissue hemodynamics (THC, SO_2 and BFI) during the whole protocol, before administering the drug and throughout all treatment at different time points. In general, the estimated pre-treatment tumor hemodynamic parameters were higher in comparison to the shoulder tissue. These findings might be associated with the overexpression of VEGF and other pro-angiogenic factors in the tumor, which allows the development of an extended vascular network [52]. This is, in fact, the basis of the contrast in the optical signals for both pre-clinical and clinical studies [18,19]. Furthermore, the estimated pre-treatment tissue hemodynamics of the treated and control groups within the tumor and shoulder locations were similar indicating an initial physiological similarity between the randomly formed therapy groups.

Beyond the characterization of the pre-treatment tissue hemodynamics of the therapy groups (treated and control) in the tumor and in the shoulder, we have also evaluated the difference between the therapy outcome groups (responder and non-responder). The log-transformed pre-treatment tumor BFI was found to be statistically significantly different between the responder and non-responder groups, whereas THC and SO_2 remained unchanged. This was then utilized to do a receiver operating characteristic (ROC) curve analysis with a logistic regression. The recovered area under the curve (AUC) obtained from log-transformed pre-treatment BFI (AUC: 0.81, p = 0.01) and that for THC & BFI (AUC: 0.79, p = 0.04) parameters provided a potential for the pre-treatment prediction of the therapy outcome. This, if confirmed, could have a potential impact for determining the usage of alternative therapeutic strategies in subjects with a high probability to not benefit from an antiangiogenic therapeutic approach. Similar results have been reported in patients with breast cancer undergoing neoadjuvant chemotherapy assessed by diffuse optical methods [53]. As per definition, biomarkers are objective, quantifiable characteristics of biological processes that measure a physiological state and may be used as surrogate endpoints to predict outcomes. Here, we suggest tumor BFI to have prediction benefit primarily in the mRCC setting and may help in the development of precision and personalized approaches.

Alongside with pre-treatment characterization, our non-invasive diffuse optical methods allowed us to carry out a longitudinal tissue hemodynamic monitoring throughout all treatment periods. The estimated tumor hemodynamics (THC, SO2 and BFI) were found to be different in the therapy and control groups, while the control location, i.e. the shoulder muscle, did not show a similar evaluation with time. These results demonstrate, first, that the hypothesized sunitinib-derived hemodynamic changes are observable, and, second, the suitability of diffuse optical methods as a tool for assessing and linking those changes to the therapeutic effects. We note that our methodology led to increased variability in optical measurements due to inherent tumor growth and probe positioning over the course of treatment; however, we have demonstrated

the value of our method to obtain scientifically relevant results despite such constraints, thus increasing the impact of the study. Besides, our findings suggest the tissue specificity of sunitinib antiangiogenic drug, which effectively alters tumor regions while avoiding global vascular changes and, thus, reduces side effects.

We have also evaluated whether the longitudinal evolution of these parameters revealed any patterns between the responder and non-responder groups early-on. The estimated tumor oxygen saturation (SO$_2$) discriminated between responder and non-responder groups from day fourteen onward. This suggests that vascular trimming is present in the responder group but absent in non-responder tumors, which might effectively modulate nutrients and oxygen supply to the tumor under antiangiogenic treatment. In this regard, although the tumor total hemoglobin concentration (THC) did not change among therapy outcomes over time, a decaying trend in both responder and non-responder groups was observed reaching a plateau region comprising from day seven of treatment onwards in both groups. This finding is in agreement with the time point reported by Zhou *et al.* in a pre-clinical SF188V + human glioma xenograft mouse model treated with sunitinib under the same dosage as our work [54]. This effect might be associated with the vascular trimming of the permeable neovasculature caused by the blockage of the VEGF signaling pathway [55]. Interestingly, tumor THC levels from the responder and non-responder groups at the plateau region matches their corresponding THC values in the shoulder position. These results might indicate that even though the blood volume level in the tumor is comparable to that of a healthy tissue due to the vascular trimming induced by the VEGF blockage, other signaling pathways or different mechanisms could potentially be interfering in the tumor development and leading to eventual acquired treatment resistance.

Besides these findings, the early tumor THC change observed at day three with respect to day zero, and the pre-treatment value were demonstrated to correlate with the extracted tumor weight. These results are in good agreement with the reported fractional blood volume changes associated with the therapy prognosis reported by Robinson *et al.* in a mouse model of 786-O ccRCC cells [56]. This may potentially be indicative of the capability of a resistant tumor to adapt and continue developing even under nutrient-depleted conditions [29]. Similarly, the early change (Day 3) in the retrieved tumor BFI parameter with respect to the pre-treatment value correlates with the final microvascular density. These results are in line with the studies by Huang *et al.* in a xenograft mouse model of 786-O ccRCC where an increase in the microvessel density in the tumor was found in sunitinib-resistant specimens [48].

In general, our findings suggest an early trigger effect induced by sunitinib antiangiogenic therapy on the initial days of treatment. This can be determined in pre-treatment THC and BFI tumor hemodynamic parameters, which turn out to be a potential set of predictive biomarkers of therapy outcome. Furthermore, early changes and longitudinal monitoring of THC, SO$_2$ and BFI parameters demonstrated the feasibility to predict the final therapy effects. These results might produce objective and reproducible cut-off values for assessment of their use as new predictive biomarkers. Although it is not trivial to extend the non-invasive application of diffuse optical techniques to renal carcinoma, minimally invasive approaches may be envisaged and become a helpful tool in medicine personalization.

5.   Conclusion

Diffuse optical techniques have been demonstrated to be a suitable toolbox for predicting the therapeutic resistance of a ccRCC tumor to antiangiogenic therapy from the pre-treatment time point. Furthermore, the longitudinal tissue hemodynamics monitoring provides not only the possibility to assess the therapeutic response over time but also to predict the ending point therapy effects from the early changes in the hemodynamic parameters. This set of features bridges the gap of the current translational oncology field by providing relevant biomarkers for achieving an

early identification of the intrinsic resistant tumors where alternative therapies might be applied in order to improve the therapy effects.

Disclosures. The authors declare no conflicts of interest.

Author Contributions. GJV, MM, JMD, MML and JJ conducted experiments and processed data. MM, JJ, EEVR, VNP, DRB and CV contributed to data processing. CV, OC and TD conceived the study. GJV, MM and CV prepared the manuscript draft. All authors reviewed and approved the manuscript.

Data availability. Data underlying the results presented in this paper are not publicly available at this time but may be obtained from the authors upon reasonable request.

Supplemental document. See Supplement 1 for supporting content.

References

1. F. Bray, M. Laversanne, H. Sung, *et al.*, "Global cancer statistics 2022: GLOBOCAN estimates of incidence and mortality worldwide for 36 cancers in 185 countries," CA: A Cancer J. Clinicians **74**(3), 229–263 (2024).
2. J. J. Hsieh, M. P. Purdue, S. Signoretti, *et al.*, "Renal cell carcinoma," Nat. Rev. Dis. Primers **3**(1), 17009 (2017). doi:10.1038/nrdp.2017.9
3. K. Gupta, J. D. Miller, J. Z. Li, *et al.*, "Epidemiologic and socioeconomic burden of metastatic renal cell carcinoma (mRCC): A literature review," Cancer Treat. Rev. **34**(3), 193–205 (2008).
4. A. Bamias, B. Escudier, C. N. Sternberg, *et al.*, "Current clinical practice guidelines for the treatment of renal cell carcinoma: a systematic review and critical evaluation," The Oncol. **22**(6), 667–679 (2017).
5. R. J. Motzer, T. E. Hutson, P. Tomczak, *et al.*, "Sunitinib versus Interferon Alfa in Metastatic Renal-Cell Carcinoma," N. Engl. J. Med. **356**(2), 115–124 (2007). doi:10.1056/NEJMoa065044
6. L. M. Ellis and D. J. Hicklin, "VEGF-targeted therapy: mechanisms of anti-tumour activity," Nat. Rev. Cancer **8**(8), 579–591 (2008).
7. B. I. Rini, "Vascular endothelial growth factor-targeted therapy in metastatic renal cell carcinoma," Cancer **115**(S10), 2306–2312 (2009).
8. C. Morais, "Sunitinib resistance in renal cell carcinoma," J. Kidney Cancer VHL **1**(1), 1–11 (2014).
9. B. I. Rini and M. B. Atkins, "Resistance to targeted therapy in renal-cell carcinoma," The Lancet Oncol. **10**(10), 992–1000 (2009).
10. J. C. van der Mijn, J. W. Mier, H. J. Broxterman, *et al.*, "Predictive biomarkers in renal cell cancer: Insights in drug resistance mechanisms," Drug Resist. Updates **17**(4-6), 77–88 (2014).
11. F. Donskov, M. D. Michaelson, I. Puzanov, *et al.*, "Sunitinib-associated hypertension and neutropenia as efficacy biomarkers in metastatic renal cell carcinoma patients," Br. J. Cancer **113**(11), 1571–1580 (2015).
12. C. S. Harmon, S. E. DePrimo, R. A. Figlin, *et al.*, "Circulating proteins as potential biomarkers of sunitinib and interferon-α efficacy in treatment-naïve patients with metastatic renal cell carcinoma," Cancer Chemother Pharmacol. **73**(1), 151–161 (2014).
13. R. K. Jain, D. G. Duda, C. G. Willett, *et al.*, "Biomarkers of response and resistance to antiangiogenic therapy," Nat. Rev. Clin. Oncol. **6**(6), 327–338 (2009).
14. C. Kelly-Morland, S. Rudman, P. Nathan, *et al.*, "Evaluation of treatment response and resistance in metastatic renal cell cancer (mRCC) using integrated 18F-Fluorodeoxyglucose (18F-FDG) positron emission tomography/magnetic resonance imaging (PET/MRI); The REMAP study," BMC Cancer **17**(1), 392 (2017).
15. V. Pankowska, B. Malkowski, M. Wedrowski, *et al.*, "FDG PET/CT as a survival prognostic factor in patients with advanced renal cell carcinoma," Clin. Exp. Med. **19**(1), 143–148 (2019).
16. J. Jin, Y. Xie, J.-S. Zhang, *et al.*, "Sunitinib resistance in renal cell carcinoma: From molecular mechanisms to predictive biomarkers," Drug Resist. Updates **67**, 100929 (2023).
17. T. Durduran, R. Choe, W. B. Baker, *et al.*, "Diffuse Optics for Tissue Monitoring and Tomography," Rep. Prog. Phys. **73**(7), 076701 (2010).
18. R. Choe and T. Durduran, "Diffuse optical monitoring og the neoadjuvant breast cancer therapy," IEEE J. Select. Topics Quantum Electron. **18**(4), 1367–1386 (2012).

19. C. Zhou, R. Choe, N. Shah, *et al.*, "Diffuse optical monitoring of blood flow and oxygenation in human breast cancer during early stages of neoadjuvant chemotherapy," J. Biomed. Opt. **12**(5), 051903 (2007).

20. G. Ramirez, A. R. Proctor, K. W. Jung, *et al.*, "Chemotherapeutic drug-specific alteration of microvascular blood flow in murine breast cancer as measured by diffuse correlation spectroscopy," Biomed. Opt. Express **7**(9), 3610 (2016).

21. P. Farzam, J. Johansson, M. Mireles, *et al.*, "Pre-clinical longitudinal monitoring of hemodynamic response to anti-vascular chemotherapy by hybrid diffuse optics," Biomed. Opt. Express **8**(5), 2563 (2017).

22. C. Menon, G. M. Polin, I. Prabakaran, *et al.*, "An integrated approach to measuring tumor oxygen status using human melanoma xenografts as a model," Cancer Res. **63**(21), 7232–7240 (2003).

23. U. Sunar, S. Makonnen, C. Zhou, *et al.*, "Hemodynamic responses to antivascular therapy and ionizing radiation assessed by diffuse optical spectroscopies," Opt. Express **15**(23), 15507 (2007).

24. B. J. Tromberg, Z. Zhang, A. Leproux, *et al.*, "Predicting responses to neoadjuvant chemotherapy in breast cancer: ACRIN 6691 trial of diffuse optical spectroscopic imaging," Cancer Res. **76**(20), 5933–5944 (2016).

25. J. M. Cochran, S. H. Chung, A. Leproux, *et al.*, "Longitudinal optical monitoring of blood flow in breast tumors during neoadjuvant chemotherapy," Phys. Med. Biol. **62**(12), 4637–4653 (2017).

26. U. Sunar, H. Quon, T. Durduran, *et al.*, "Noninvasive diffuse optical measurement of blood flow and blood oxygenation for monitoring radiation therapy in patients with head and neck tumors: a pilot study," J. Biomed. Opt. **11**(6), 064021 (2006).

27. L. Dong, M. Kudrimoti, D. Irwin, *et al.*, "Diffuse optical measurements of head and neck tumor hemodynamics for early prediction of chemoradiation therapy outcomes," J. Biomed. Opt. **21**(8), 085004 (2016).

28. G. Yu, T. Durduran, C. Zhou, *et al.*, "Real-time in situ monitoring of human prostate photodynamic therapy with diffuse light," Photochem. Photobiol. **82**(5), 1279–1284 (2006).

29. G. Jiménez-Valerio, M. Martínez-Lozano, N. Bassani, *et al.*, "Resistance to antiangiogenic therapies by metabolic symbiosis in renal cell carcinoma PDX models and patients," Cell Rep. **15**(6), 1134–1143 (2016).

30. M. Pàez-Ribes, E. Allen, J. Hudock, *et al.*, "Antiangiogenic therapy elicits malignant progression of tumors to increased local invasion and distant metastasis," Cancer Cell **15**(3), 220–231 (2009).

31. C. A. Schneider, W. S. Rasband, and K. W. Eliceiri, "NIH Image to ImageJ: 25 years of image analysis," Nat. Methods **9**(7), 671–675 (2012).

32. M. Mireles, J. Morales-Dalmau, J. D. Johansson, *et al.*, "Non-invasive and quantitative in vivo monitoring of gold nanoparticle concentration and tissue hemodynamics by hybrid optical spectroscopies," Nanoscale **11**(12), 5595–5606 (2019).

33. M. S. Patterson, S. Andersson-Engels, B. C. Wilson, *et al.*, "Absorption spectroscopy in tissue-simulating materials: a theoretical and experimental study of photon paths," Appl. Opt. **34**(1), 22–30 (1995).

34. K. Vishwanath, H. Yuan, W. T. Barry, *et al.*, "Using optical spectroscopy to longitudinally monitor physiological changes within solid tumors," Neoplasia **11**(9), 889–900 (2009).

35. A. Jules, D. Means, J. R. Troncoso, *et al.*, "Diffuse reflectance spectroscopy of changes in tumor microenvironment in response to different doses of radiation," Radiat. Res. **198**(6), 545–552 (2022). doi:10.1667/RADE-21-00228.1

36. D. R. Busch, W. Guo, R. Choe, *et al.*, "Computer aided automatic detection of malignant lesions in diffuse optical mammography," Med. Phys. **37**(4), 1840–1849 (2010).

37. G. Lupo, N. Caporarello, M. Olivieri, *et al.*, "Anti-angiogenic therapy in cancer: downsides and new pivots for precision medicine," Front. Pharmacol. **7**, 1 (2017).

38. I. Dagogo-Jack and A. T. Shaw, "Tumour heterogeneity and resistance to cancer therapies," Nat. Rev. Clin. Oncol. **15**(2), 81–94 (2018).

39. H.-W. Wang, T. C. Zhu, M. E. Putt, *et al.*, "Broadband reflectance measurements of light penetration, blood oxygenation, hemoglobin concentration, and drug concentration in human intraperitoneal tissues before and after photodynamic therapy," J. Biomed. Opt. **10**(1), 014004 (2005).

40. E. U. Cidon, P. Alonso, and B. Masters, "Markers of response to antiangiogenic therapies in colorectal cancer: where are we now and what should be next?" Clin. Med. Insights Oncol. **10**(Suppl 1), CMO.S34542 (2016).

41. G. Reyes, A. Villanueva, C. García, *et al.*, "Orthotopic xenografts of human pancreatic carcinomas acquire genetic aberrations during dissemination in nude mice," Cancer Res. **56**(24), 5713–5719 (1996).

42. G. Capellá, L. Farré, A. Villanueva, *et al.*, "Orthotopic models of human pancreatic cancer," Ann. NY Acad. Sci. **880**(1), 103–109 (1999).

43. G. S. Papaetis and K. N. Syrigos, "Sunitinib: a multitargeted receptor tyrosine kinase inhibitor in the era of molecular cancer therapies," BioDrugs **23**(6), 377–389 (2009).

44. A. M. Grimaldi, T. Guida, R. D'Attino, *et al.*, "Sunitinib: bridging present and future cancer treatment," Annals Oncology **18**, vi31–vi34 (2007).

45. M. M. Vickers, T. K. Choueiri, M. Rogers, *et al.*, "Clinical outcome in metastatic renal cell carcinoma patients after failure of initial vascular endothelial growth factor-targeted therapy," Urology **76**(2), 430–434 (2010).

46. J. Busch, C. Seidel, S. Weikert, *et al.*, "Intrinsic resistance to tyrosine kinase inhibitors is associated with poor clinical outcome in metastatic renal cell carcinoma," BMC Cancer **11**(1), 295 (2011).

47. S. H. Lim, I. G. Hwang, J. H. Ji, *et al.*, "Intrinsic resistance to sunitinib in patients with metastatic renal cell carcinoma," Asia-Pac. J. Clin. Oncol. **13**(1), 61–67 (2017).

48. D. Huang, Y. Ding, M. Zhou, *et al.*, "Interleukin-8 mediates resistance to antiangiogenic agent sunitinib in renal cell carcinoma," Cancer Res. **70**(3), 1063–1071 (2010).

49. G. Bergers and D. Hanahan, "Modes of resistance to anti-angiogenic therapy," Nat. Rev. Cancer **8**(8), 592–603 (2008).

50. L. Moserle, G. Jiménez-Valerio, and O. Casanovas, "Antiangiogenic therapies: Going beyond their limits," Cancer Discovery **4**(1), 31–41 (2014).

51. D. B. Mendel, A. D. Laird, X. Xin, *et al.*, "In vivo antitumor activity of SU11248, a novel tyrosine kinase inhibitor targeting vascular endothelial growth factor and platelet-derived growth factor receptors: Determination of a pharmacokinetic/pharmacodynamic relationship," Clin. Cancer Res. **9**(1), 327–337 (2003).

52. A. Takahashi, H. Sasaki, S. J. Kim, *et al.*, "Markedly increased amounts of messenger RNAs for vascular endothelial growth factor and placenta growth factor in renal cell carcinoma associated with angiogenesis," Cancer Res. **54**(15), 4233–4237 (1994).

53. W. T. Tran, M. J. Gangeh, L. Sannachi, *et al.*, "Predicting breast cancer response to neoadjuvant chemotherapy using pretreatment diffuse optical spectroscopic texture analysis," Br. J. Cancer **116**(10), 1329–1339 (2017).

54. Q. Zhou, P. Guo, and J. M. Gallo, "Impact of angiogenesis inhibition by sunitinib on tumor distribution of temozolomide," Clin. Cancer Res.. **14**(5), 1540–1549 (2008).

55. G. Neufeld, T. Cohen, S. Gengrinovitch, *et al.*, "Vascular endothelial growth factor (VEGF) and its receptors," FASEB J. **13**(1), 9–22 (1999).

56. S. P. Robinson, J. K. R. Boult, N. S. Vasudev, *et al.*, "Monitoring the vascular response and resistance to sunitinib in renal cell carcinoma in vivo with susceptibility contrast MRI," Cancer Res. **77**(15), 4127–4134 (2017).